



Characterization of large format lithium ion battery exposed to extremely high temperature

Xuning Feng ^{a, b}, Jing Sun ^b, Minggao Ouyang ^{a,*}, Xiangming He ^{a, c}, Languang Lu ^a, Xuebing Han ^a, Mou Fang ^c, Huei Peng ^d

^a State Key Laboratory of Automotive Safety and Energy, Tsinghua University, Beijing 100084, China

^b Department of Naval Architecture and Marine Engineering, University of Michigan, Ann Arbor, MI 48109, USA

^c Institute of Nuclear and New Energy Technology, Tsinghua University, Beijing 100084, China

^d Department of Mechanical Engineering, University of Michigan, Ann Arbor, MI 48109, USA



HIGHLIGHTS

- Fading mechanisms for large Li-ion battery during a thermal runaway were studied.
- EV-ARC test was terminated before thermal runaway to study the fading mechanism.
- The separator melting point dictates the reusability of the battery after heating.
- Cycled after heating, the lost capacity of the battery may be recovered partially.
- Capacity loss was analyzed using ICA and discussed using a mechanistic model.

ARTICLE INFO

Article history:

Received 24 May 2014

Received in revised form

2 August 2014

Accepted 22 August 2014

Available online 2 September 2014

Keywords:

Lithium ion battery

Thermal runaway

High temperature capacity fading

Incremental capacity analysis

Battery safety

ABSTRACT

This paper provides a study on the characterizations of large format lithium ion battery cells exposed to extreme high temperature but without thermal runaway. A unique test is set up: an extended volume-accelerating rate calorimetry (EV-ARC) test is terminated at a specific temperature before thermal runaway happens in the battery. The battery was cooled down after an EV-ARC test with early termination. The performances of the battery before and after the EV-ARC test are investigated in detail. The results show that (a) the melting point of the separator dictates the reusability of the 25 Ah NCM battery after a near-runaway event. The battery cannot be reused after being heated to 140 °C or higher because of the exponential rise in ohmic resistance; (b) a battery can lose up to 20% of its capacity after being heated to 120 °C just one time; (c) if a battery is cycled after a thermal event, its lost capacity may be recovered partially. Furthermore, the fading and recovery mechanisms are analyzed by incremental capacity analysis (ICA) and a prognostic/mechanistic model. Model analysis confirms that the capacity loss at extremely high temperature is caused by the increase of the resistance, the loss of lithium ion (LLI) at the anode and the loss of active material (LAM) at the cathode.

© 2014 Elsevier B.V. All rights reserved.

1. Introduction

Lithium ion batteries are the prevailing choices to power today's electric vehicles (EV), because of its high energy/power density and long cycle life compared with other choices. However, incidents such as battery fires after crashes have attracted much attention [1–3] and given rise to public concerns about the safety of the

lithium ion batteries. Thermal runaway behavior is an important research topic which has been at the center of safety events.

Large format battery is of particular interest because of their increasing popularity in production of electric vehicles. Large format batteries have the advantages of reduced cell number and pack complexity [4], which lead to the improved reliability of a battery pack [5]. However, a large format battery is more vulnerable to thermal runaway because it contains more stored energy. Cooling is less effective because of its lower surface/volume ratio, which leads to higher non-uniformity of temperature distribution within the cell [5].

Batteries with $\text{LiNi}_x\text{Co}_y\text{Mn}_z\text{O}_2$ (NCM) cathode are promising for EV applications. NCM cathode material demonstrates higher

* Corresponding author. Tel.: +86 10 62773437; fax: +86 10 62785708.

E-mail addresses: fxn07@mails.tsinghua.edu.cn (X. Feng), ouymg@tsinghua.edu.cn (M. Ouyang).

capacity, lower cost and less toxicity within the family of Li-ion batteries [6,7]. In thermal runaway tests, batteries with NCM cathode perform better than those with LiCoO₂ (LCO) and LiNi_{0.8}-Co_{0.15}Al_{0.05}O₂ (NCA) do, but worse than those with LiMn₂O₄ (LMO) and LiFePO₄ (LFP) [8]. Nevertheless, the NCM cathode shows better high temperature durability and higher specific capacity than LMO and higher energy density than LFP [8].

We have reported the thermal runaway features of large format prismatic lithium ion battery with NCM cathode using extended volume accelerating rate calorimetry (EV-ARC) in Ref. [9]. The thermal runaway process for the specific NCM large format battery has been divided into 6 stages based on the general knowledge from those reviews [10–14] of Li-ion battery safety. In Stage I, the capacity fades at high temperature (>50 °C). In Stage II, the solid electrolyte interface (SEI) decomposition starts and releases detectable heat if the reaction continues [15–21]. And it should be noted that the SEI decomposition will continue to a temperature as high as 250 °C (ends at Stage IV) [20,21]. Losing its protection layer, the lithium intercalated in anode starts to react with the electrolyte [15,17,20–22]. In Stage III, the separator melting causes a decrease in temperature rise rate as the temperature goes higher (120 °C–140 °C). In Stage IV (140 °C–240 °C), some cathode materials start to react with the electrolyte and release heat [5,23–25], while the NCM cathode seems to be strong enough not to react until the temperature reaches 240 °C or higher [26–31].

Besides thermal runaway, batteries may experience “near” thermal runaway conditions where they are exposed to extreme temperature beyond the limit set by a battery management system. To understand the safety features of the battery and to characterize the impact of the high temperature exposure on the battery performance, we investigate the status of the battery at different specific high temperature near thermal runaway point. We try to “freeze” the battery during a thermal runaway test like P. Roeder et al. did in Ref. [32] using an interrupted ARC test to see what the behavior of a large format battery is after being exposed to extreme high temperature before thermal runaway. It is indicated that high temperature capacity fading will happen as reported in Refs. [33–37]. Therefore, we can exploit previous mechanistic/prognostic methods to analyze and quantify the capacity degradation of a battery exposed to extremely high temperature.

Capacity degradation for lithium ion battery is mainly caused by the loss of cyclable lithium inventory (LLI) and the loss of active material (LAM) [38–44]. As shown in Refs. [42], the LLI at anode happens first, followed by the LAM at cathode as temperature rises. The LLI is mainly caused by the SEI decomposition and the anode reaction with electrolyte, while the LAM is mainly caused by the cathode decomposition. To analyze LLI and LAM, a parameterized prognostic and mechanistic model presented in Refs. [38,39,43–50] can be used, whose parameters are linked directly to certain capacity fading mechanisms. In such a prognostic and mechanistic model, the capacity loss can be quantified in simulation by selecting proper stoichiometric coefficient x and y in Li_xC_6 and $\text{Li}_y\text{Ni}_a\text{Co}_b\text{Mn}_c\text{O}_2$, respectively [39,43]. Moreover, incremental capacity analysis (ICA) has been used to analyze battery aging data and interpret the capacity fading mechanisms in many publications [51–59].

In this paper, we have investigated the characterization of large format lithium ion battery after suffering a short period of high temperature exposure. The battery was heated to an extremely high temperature using EV-ARC then cooled down before it runs into thermal runaway. The voltage drop and internal resistance rise during heating were quantified. The reusability of the 25 Ah NCM battery was evaluated by its discharge capacity. Scanning electron microscope (SEM) was employed to find the influence of the melting point of the separator on the reusability of the 25 Ah NCM

battery. The capacity fading mechanisms were analyzed using ICA, and discussed using a prognostic/mechanistic model.

2. Experiment

2.1. An EV-ARC test with early termination

This work is a follow-up work of [9]. The battery was heated by an EV-ARC (Fig. 1), manufactured by Thermal Hazard Technology®. The functions of the EV-ARC are essentially the same as those pervasively used ARC. A common EV-ARC test also follows the heat-wait-seek method. The difference is that the calorimeter of the EV-ARC is much larger than that of the standard ARC. The selected EV-ARC can hold a large format battery with a capacity of 25 Ah investigated in this paper.

The 25 Ah battery employed for the EV-ARC test is a rechargeable $\text{LiNi}_x\text{Co}_y\text{Mn}_z\text{O}_2$ polymer battery manufactured by AE Energy Co. Ltd. It has $\text{LiNi}_x\text{Co}_y\text{Mn}_z\text{O}_2$ as its cathode and graphite as its anode. The separator is polyethylene (PE) based with ceramic coating. We have reported differential scanning calorimetry test result on the separator in our previous research in Ref. [9]. The detailed material composition of the battery is shown in Fig. 2.

Fig. 3 shows the locations of the thermal couples as reported in Ref. [9]. Table 1 summarizes the setup of all the EV-ARC tests. Battery No. 1 and No. 2 were installed with a thermal-couple TC_1 inserted inside the battery, as in Ref. [9]. Note that our previous research has established that for the EV-ARC test following the heat-wait-seek approach, the maximum temperature difference within the battery does not exceed 1 °C for 97% of the time during a thermal runaway test [9]. Therefore, no thermal couple is used for internal temperature measurement in most of our tests. Temperature data measured by thermal couple No. 2 (TC_2), which is representative of the internal temperature of the battery under the uniform temperature distribution condition, is used for thermal analysis in the following sections.

A unique test, which is called EV-ARC test with early termination, is set up to study the fading mechanisms for lithium ion battery exposed to extreme high temperature and “near” runaway conditions. In the EV-ARC test with early termination, the heating process was stopped once the temperature reaches a pre-defined value. The battery was pulled out of the chamber and a fan was



Fig. 1. Picture of the EV-ARC used for this research.

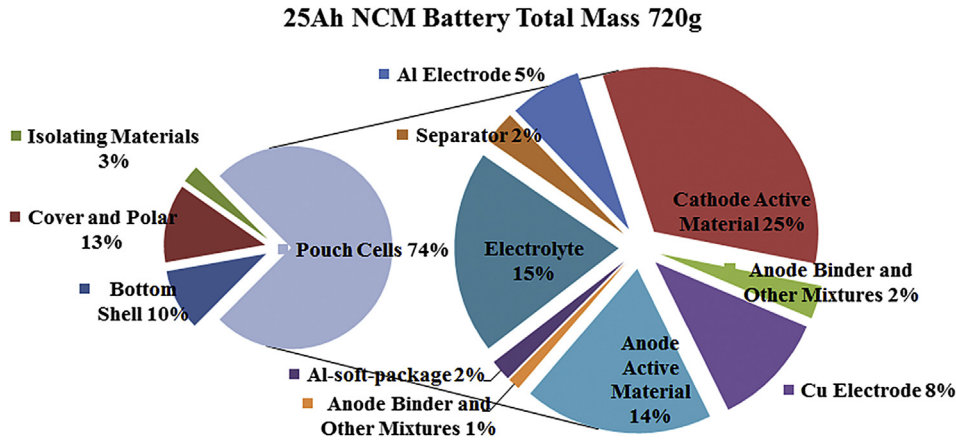


Fig. 2. The components of the 25 Ah NCM battery.

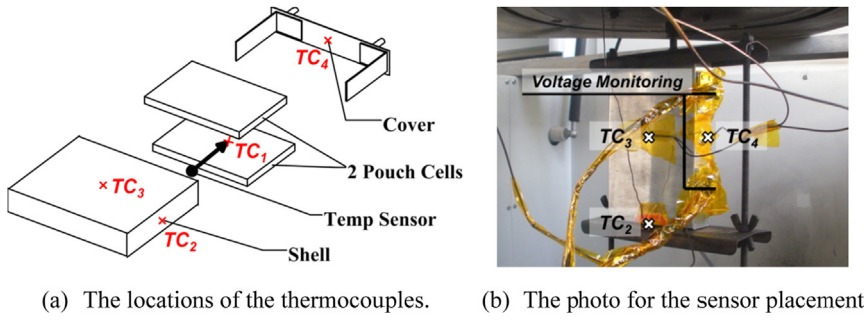


Fig. 3. Thermal couple placement for the EV-ARC test with early termination.

used for forced cooling, as shown in Fig. 4(a). In such a forced cooling process, the battery was expected to be cooled down to ambient temperature within 90 min, and the cooling process has been found to be reproducible.

The fading mechanism of the battery heated to different stages in a thermal runaway test can be studied through such a forced cooling. T_{cool} is the terminal temperature of the heating process, and is selected to be within Stage I ~ IV of the thermal runaway process as defined in Ref. [9] and shown in Fig. 4(b). Here T_{cool} was selected to satisfy $T_1 \leq T_{cool} \leq T_3$ (where T_1 and T_3 are shown in Fig. 4(b)) and the selected values are {80 °C, 90 °C, 100 °C, 110 °C, 120 °C, 130 °C, 140 °C, 160 °C}. T_1 is the temperature when the temperature rising rate of the battery exceed $0.01\text{ }^{\circ}\text{C min}^{-1}$, which is the detected sensitivity of EV-ARC. In other words, T_1 is the temperature when the heat generation of the battery caused by side reactions is detectable. T_3 is the onset temperature of thermal runaway, after which the temperature rises exponentially. We choose $T_1 \leq T_{cool} \leq T_3$ in order to investigate the characterization of the battery after being exposed to extremely high temperature but not reached thermal runaway.

Table 1 summarizes the setup of the EV-ARC tests with early termination, the tests were repeated for eight batteries with different values of T_{cool} . Note that the voltage was also monitored throughout the EV-ARC test with early termination as in Fig. 3(b). A pulse charge/discharge profile (as shown in Fig. 4(c)) was applied to study the variation of the internal resistance during the entire process, like T. Yoshida et al. did in Ref. [37]. Fig. 4(c) shows the temperature and voltage curve for one of the EV-ARC tests with early termination. The temperature keeps rising until the cooling starts at 120 °C. Meanwhile the voltage drops continuously with symmetric pulse charge/discharge.

Table 1 also shows that pulse charge/discharge profile was not conducted on the first two batteries. Battery No. 3 was tested by different pulse currents. All of the batteries have been charged to full SOC with an initial voltage of 4.17–4.18 V before heating.

2.2. The performance test

Performance tests were conducted before and after the ARC tests, with a constant current of 5 A (C/5), see Fig. 5 and Table 2. In Section 3.5, further ICA is performed on those C/5 discharge data sets.

3. Results and discussions

3.1. The voltage drop after being heated

Fig. 6 shows the initial voltage and the terminal voltage for EV-ARC tests that were terminated at different temperatures T_{cool} . The

Table 1
Experiment settings for an EV-ARC test with early termination.

No.	$T_{cool}/^{\circ}\text{C}$	With thermal couple TC_1 inside?	With pulse charge/discharge?	Pulse current/A	Initial voltage/V
1	80	Y	N	/	4.1753
2	90	Y	N	/	4.1722
3	100	N	Y	0.5	4.1747
4	110	N	Y	0.25	4.1738
5	120	N	Y	0.25	4.1753
6	130	N	Y	0.25	4.1760
7	140	N	Y	0.25	4.1794
8	160	N	Y	0.25	4.1800

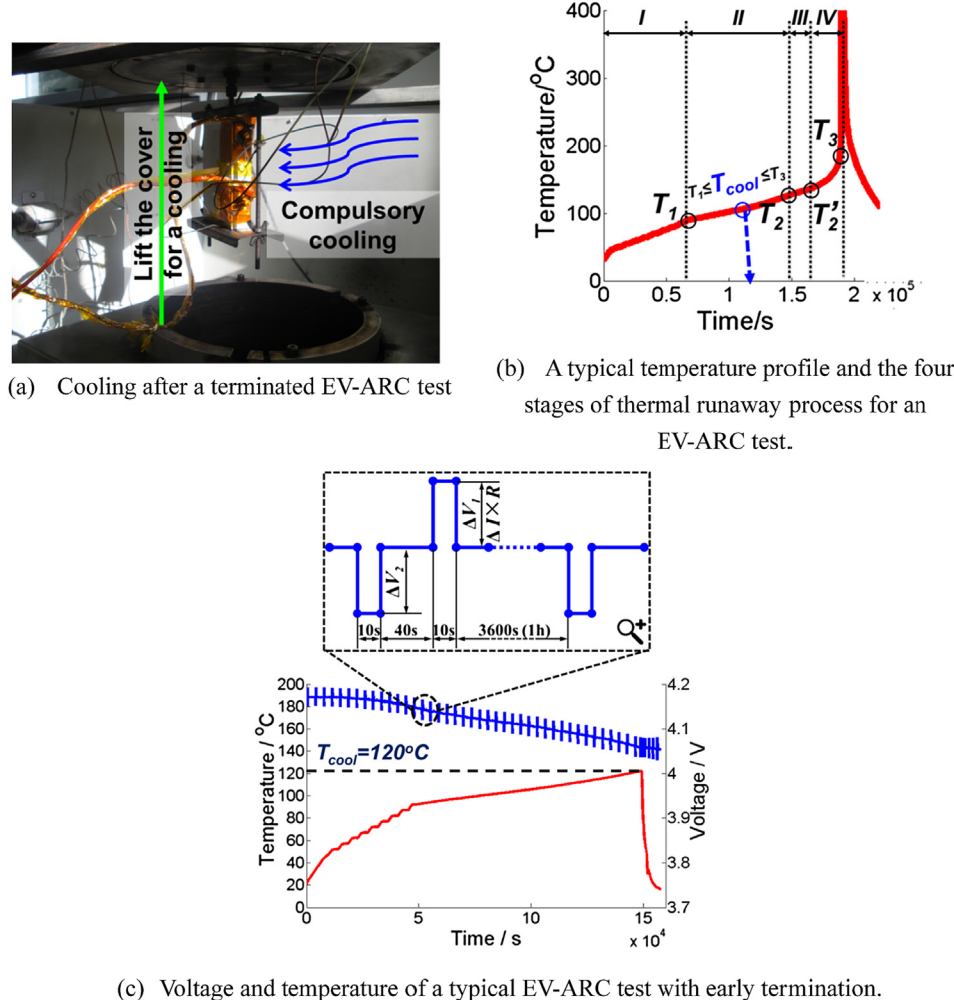


Fig. 4. A typical EV-ARC test with early termination.

terminal voltage drops as heating process is extended and T_{cool} rises. A linear curve fitting was performed for the terminal voltage in Fig. 6. A constant slope $dV/dT_{cool} = -0.002877 \text{ V K}^{-1}$ can be observed.

3.2. The variation of the internal resistance

As the battery went through the heating process, internal resistance and capacity were both affected. The variation of the

internal resistance was investigated using pulse current charge/discharge profile as shown in Fig. 4(c). The internal resistance R_{in} is defined as the quotient of the average pulse voltage and the pulse current, Eq. (1). $\Delta V_1(\Delta V_2)$ is the pulse voltage rise (drop) shown in Fig. 4(c).

$$R_{in} = (\Delta V_1 + \Delta V_2)/(2\Delta I) \quad (1)$$

Fig. 7 shows the variations of battery internal resistance during the heating/cooling process for Experiment No. 6 in Table 1, where $T_{cool} = 130^\circ\text{C}$. R_{in} rises from $82.7 \text{ m}\Omega$ to $95.0 \text{ m}\Omega$ during the heating process. However, R_{in} increases sharply to $214.2 \text{ m}\Omega$ after the battery was cooled down to ambient. Table 3 collects R_{in} before heating, after heating but before cooling, and after cooling. It is interesting to

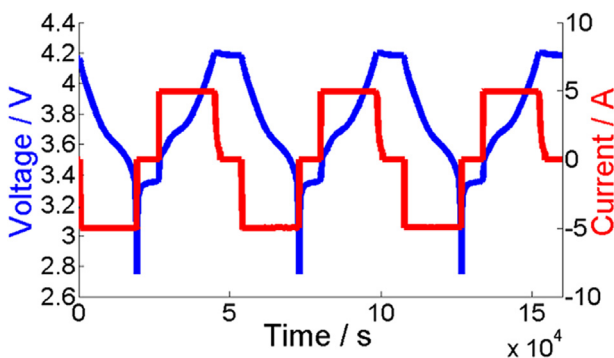


Fig. 5. The performance test profile.

Table 2
Profile for the performance test.

Step no.	Step name	Duration	Condition	Cycle no.
1	Rest	10 min		
2	Discharge		5 A (C/5) until 2.75 V	
3	Rest	90 min		
4	Constant current charge		5 A (C/5) until 4.2 V	
5	Constant voltage charge		4.2 V until $I < 0.05 \text{ A}$	
6	Rest	90 min		
7	Cycle, step 2–6			N
8	End			

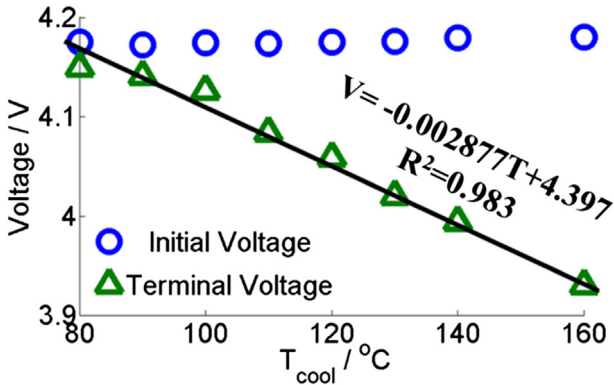


Fig. 6. The voltage before and after an EV-ARC test with early termination.

note that no significant rises were observed towards the end of heating and before the cooling started, while R_{in} displays a sharp rise after the cooling started for $T_{cool} \geq 120$ °C. The PE-based separator inside the battery melts in a range of 120–140 °C as reported in Ref. [9]. For $T_{cool} = 130$ °C (140 °C), R_{in} after cooling down is shown an increase of 159.0% (210%) of the initial value before heating. However, R_{in} only increases by 14.9% (14.8%) before cooling down. In addition, for $T_{cool} = 160$ °C, R_{in} shows a prominent increase of 1343.8%. Given that the rise of internal resistance only happened after cooling started, it seems that the separator shutdown did not happen at high temperature but was activated by the cool down process.

R_{in} determines how much energy the battery can be re-filled with a fixed charging current of $I = 5$ A in this case and how much power the battery can output. Note that the battery should operate within a voltage range of 2.75 V–4.2 V (i.e., a maximum voltage difference of $4.2 - 2.75 = 1.45$ V) defined in the manual of the 25 Ah battery provided by the manufacturer, the maximum internal resistance permitted for charge/discharge cycle should be less than $1.45\text{ V}/5\text{ A} = 0.290\text{ }\Omega = 290\text{ m}\Omega$, considering the current $I = 5\text{ A}$ in Table 2. Therefore the battery was not reusable after being cooled down from 160 °C, as will be further discussed in Section 3.4.

Despite separator melting, the thickness growth of SEI, the battery inflation and the electrolyte leakage may all contribute to the increase of R_{in} . First, the lithium intercalated in graphite anode may react with the electrolyte at high temperature [20,21]. Such a reaction contributes to SEI reforming that adds up the SEI thickness,

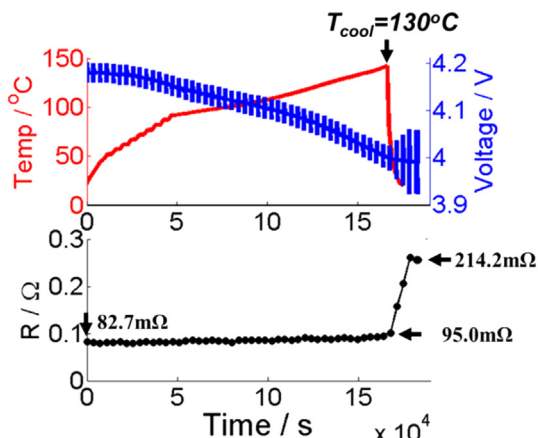


Fig. 7. The variation of the internal resistance during a typical EV-ARC test with early termination.

Table 3
The internal resistance before and after cooling.

Exp. No.	T_{cool} /°C	R_{in} before heating/mΩ	R_{in} before cooling		R_{in} after cooling/mΩ	
			mΩ	% Rise	mΩ	% Rise
4	110	102.8	115.8	12.6%	121.9	18.6%
5	120	34.1	36.5	7.0%	70.9	107.9%
6	130	82.7	95.0	14.9%	214.2	159.0%
7	140	82.6	94.8	14.8%	256	210.0%
8	160	45.2	95.5	111.3%	652.6	1343.8%

which leads to the internal resistance rise as explained in Ref. [37]. Second, note that the solvent used in the 25 Ah NCM battery gassifies at around 100–110 °C, which lead to a swell or even a leakage above 110 °C. The battery swell can cause a contact loose between the electrodes, leading to an increase of R_{in} . Third, the leaked electrolyte and solvent carried out some of the lithium within the battery, causing a nominal LLI in the analysis. In addition, the leakage may lead to insufficient electrolyte and solvent at some area on the electrode, causing a nominal LAM in the analysis and an increase of R_{in} .

3.3. SEM results for the separator

Further physical characteristics for the ceramic coated PE-based separator are reported here. The separator has two different sides: one looks smooth (Fig. 8(a)), the other looks coarse (Fig. 8(b)). The two sides can be distinguished by naked eyes. The ceramic is coated on the coarse side.

Scanning electron microscope (SEM) images for the separator were collected and the results reported in Fig. 9. The magnification time for the smooth side is 20,000, while for the coarse side is 1000. The endothermic reaction happens within a range of 120–140 °C [9]. Therefore, holes can both be seen on the smooth side for the sample before and after heated to 120 °C. However, no regular holes can be found on the smooth side after the sample was heated to 140 °C, indicating that the internal resistance rose significantly.

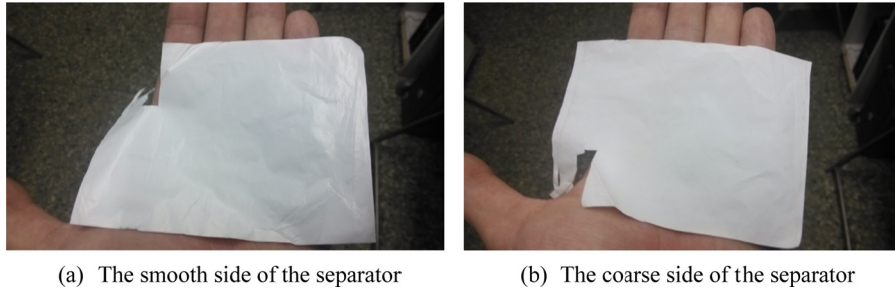
3.4. The capacity retention rate

Charge/discharge cycles, as in Table 2, were conducted on the battery after an EV-ARC test with early termination. At first, the charge/discharge cycle number defined for Step 7 of Table 2 is set to $N = 3$. The battery could recover part of its lost capacity after a few charge/discharge cycles, as the V-type curve shown in Fig. 10. The values of capacity have all been normalized to 100% according to their original values of capacity, as shown in Fig. 10. When T_{cool} rises to 110 °C or higher, the battery capacity needs more cycles to recover. Consequently, the cycle number was changed to $N = 5$ or more. The battery recovery behaviors (Fig. 10) and mechanisms are studied in detail using ICA in the following section.

Fig. 11 illustrates the recovery behavior of the battery after being heated. The battery preserves at least 60% of its initial capacity after being heated to $T_{cool} \leq 120$ °C. Furthermore, after a recovery process, the battery retains at least 80% of its original capacity following the heat-up process for $T_{cool} \leq 120$ °C. The capacity loss increases significantly above 120 °C. The increased loss of capacity was due to significant increase in internal resistance.

3.5. The incremental capacity analysis (ICA)

To understand the impact of the heating process on the capacity fading, ICA is employed to analyze the fading mechanisms for an EV-ARC test with early termination, using the method developed in Refs. [51–59].



(a) The smooth side of the separator (b) The coarse side of the separator

Fig. 8. Two sides of the separator, photos taken from a battery without going through the EV-ARC test.

Side	Before heated	Sample from battery No. 8	Sample from battery No. 11
		After heated to 120°C	After heated to 140°C
Smooth Side			
Coarse Side			

Fig. 9. SEM images for the separator.

Fig. 12 shows the IC curves for the discharge process of Experiment No. 1 ~ No. 6, representing $T_{cool} = 80^{\circ}\text{C}$, 90°C , 100°C , 110°C , 120°C and 130°C , respectively. **Fig. 12(a)–(c)** compare the IC curves before and after heating, the change is minor for those batteries heated to 80°C – 100°C . Remember that the capacity retention rates for them in **Fig. 10** are 96.9%, 94.1% and 89.1%, respectively. **Fig. 12(d)–(f)** show the IC curves for the battery heated to 110°C – 130°C . The shift of the IC curves (marked with black arrow) indicates both the capacity loss and the capacity recovery for the batteries after being heated. The convergence of the IC curves for the last few cycles indicates that after recovery the battery returned to an equilibrium state. **Fig. 12(g)** illustrates the trend of the IC curve for the first discharge cycle after the heat-up and cooling down

process, while **Fig. 12(h)** shows the data of the same batteries but for the last discharge cycles.

Here we exploited a prognostic and mechanistic model to further explain the behavior of the battery after being exposed to “near” runaway conditions. Similar model-based ICA was done by Dubarry et al. in Ref. [43] with reference made to [38,39,44–50].

The model for the discharge curve is built by Eq. (2), referring to [44]. The discharge voltage, $V_{\text{simu}}(t)$, is the difference of the cathode potential $V_{\text{ca}}(y(t))$ and the anode potential $V_{\text{an}}(x(t))$ with an ohmic potential loss of $I \cdot R$. $I = 5 \text{ A}$ is the discharge current used in the experiment, while R is the average ohmic resistance of the battery throughout the discharge process.

$$V_{\text{simu}}(t) = V_{\text{ca}}(y(t)) - V_{\text{an}}(x(t)) - I \cdot R \quad (2)$$

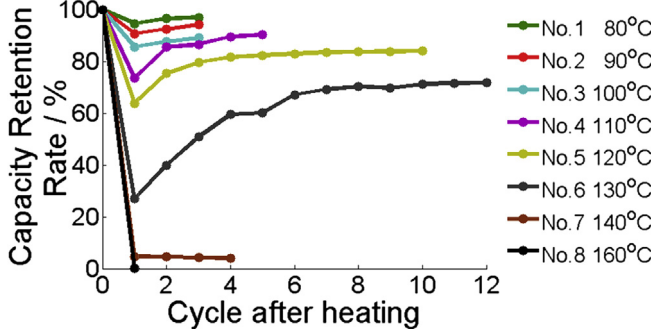


Fig. 10. The capacity recovery behavior after cooling down.

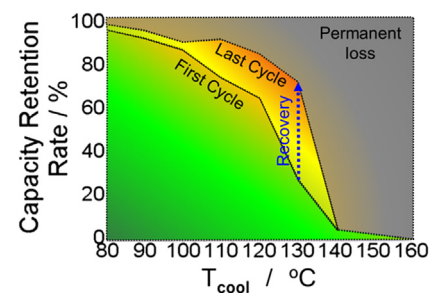


Fig. 11. The capacity recovery map.

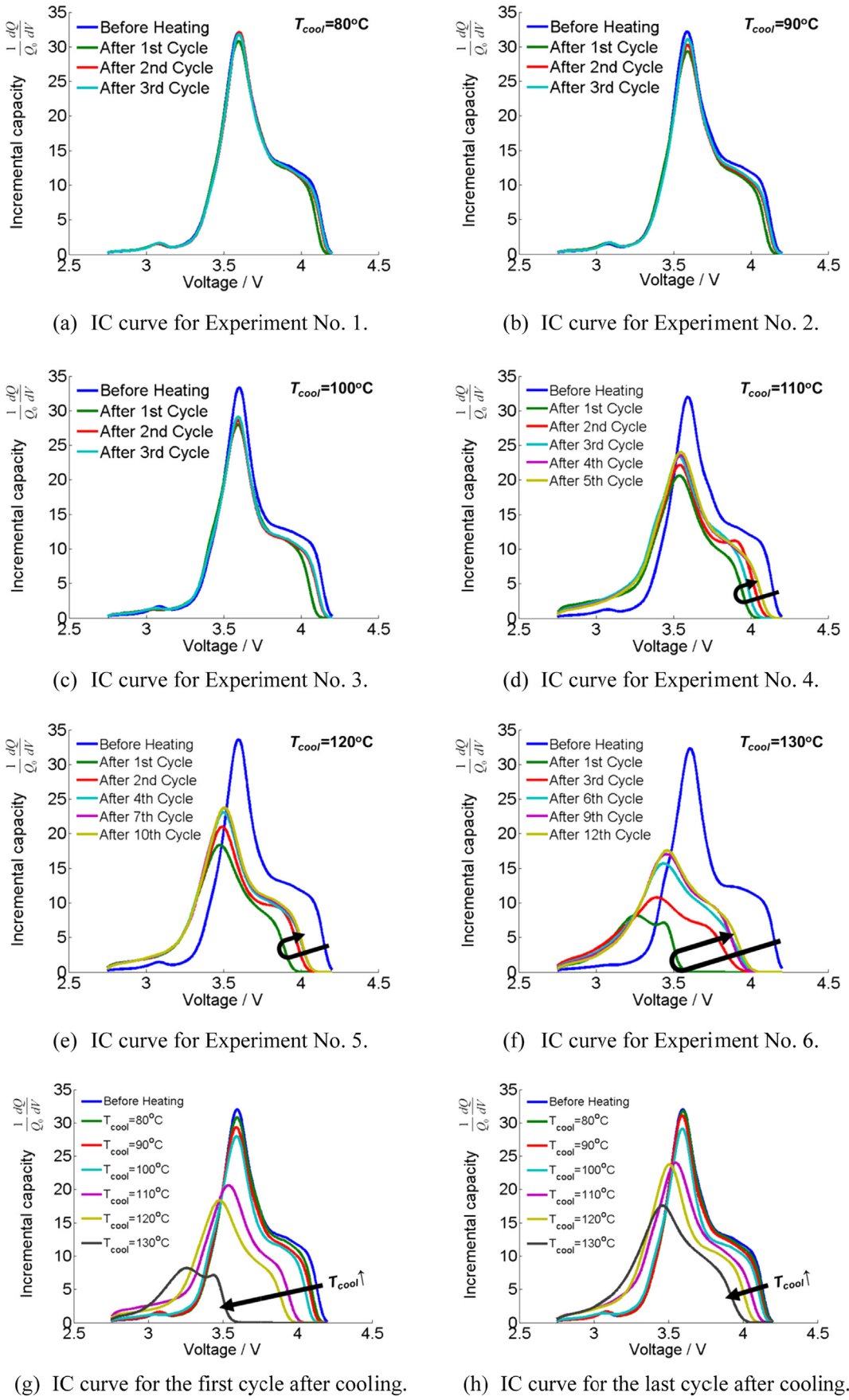


Fig. 12. ICA figures.

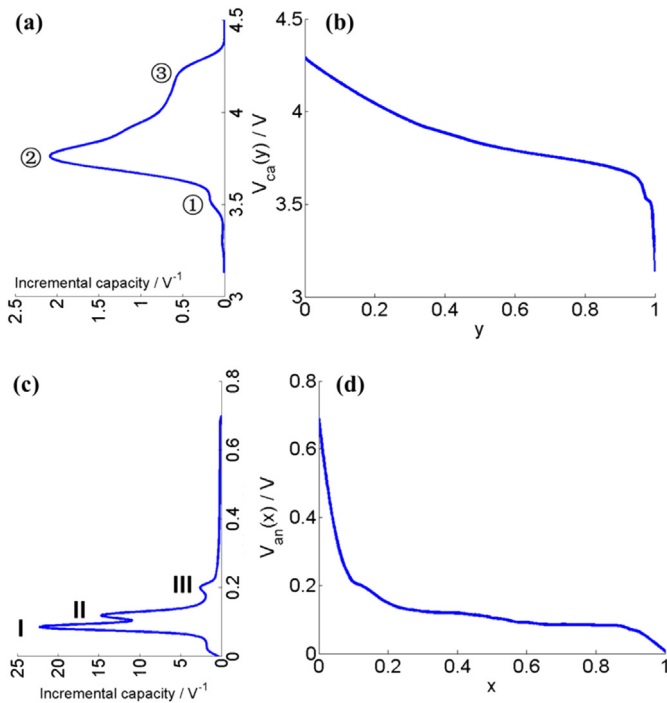


Fig. 13. The OCV and IC curve for the cathode and anode used in the model (a) IC for cathode, (b) OCV for cathode, (c) IC for anode, (d) OCV for anode.

$V_{ca}(y(t))$ and $V_{an}(x(t))$ are determined by the cathode and anode materials. $V_{ca}(y(t))$ varies with $y(t)$, while $V_{an}(x(t))$ varies with $x(t)$. Fig. 13(b) and (d) shows the cathode voltage $V_{ca}(y)$ varying with y and the anode voltage $V_{an}(x)$ varying with x used in the model, respectively. A coin cell with NCM/Li electrode was built using a piece of cathode cut from one of the 25 Ah NCM batteries to get the cathode voltage $V_{ca}(y)$. The anode OCV shown in Fig. 13(d) is consistent with that in Refs. [44,60].

Let $y(t)$ and $x(t)$ represent the state of charge (SOC) of the cathode and the anode, respectively. At the beginning of discharge, the cathode is at its low SOC ($y \rightarrow 0$) and the anode in its high SOC ($x \rightarrow 1$). As the discharge process goes on, $y(t)$ and $x(t)$ will change proportionally to the current I according to Eqs. (3) and (4), where Q_{ca} and Q_{an} are the capacity for the cathode and anode, respectively. y_0 and x_0 denote the initial value for $y(t = 0)$ and $x(t = 0)$ in the discharge process.

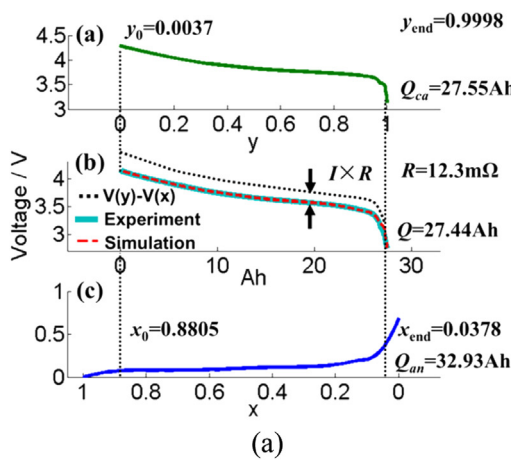


Fig. 14. Validation of the model, (a) validation of the voltage, (b) validation of the IC.

$$y(t) = y_0 + \frac{I}{Q_{ca}} \cdot t \quad (3)$$

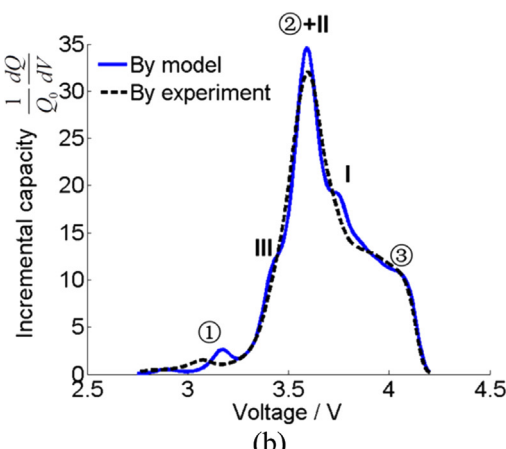
$$x(t) = x_0 - \frac{I}{Q_{an}} \cdot t \quad (4)$$

By setting proper values of $\{Q_{ca} = 27.55 \text{ Ah}, Q_{an} = 32.93 \text{ Ah}, y_0 = 0.0037, x_0 = 0.8805, R = 12.3 \text{ m}\Omega\}$, we can get a good fit of the mechanistic model with the experimental data, as shown in Fig. 14(a). The IC curve derived by the model can also fit well with that derived from the experimental data, Fig. 14(b).

The peaks seen in the IC curve reflect different phases in cathode/anode during discharging [53,54]. The cathode has three peaks marked as ①, ②, ③ in Fig. 13(a), while the anode has three peaks marked as I, II, III in Fig. 13(c). The peaks are also reflected in the IC curve derived by the model, as shown in Fig. 14(b).

Fig. 15 shows the influences of the model parameters on the shapes of IC curves. The characteristics of the IC curve change caused by specific parameter change have been defined as abbreviations in Table 4. Fig. 15(a) and (b) show that the IC curve will maintain its shape and shift to lower voltage as R increases (marked as $R \uparrow$). The IC curve shift to the lower (higher) voltage is marked as SL (SH) in Table 4. Fig. 15(c) and (d) show that when Q_{ca} decreases (marked as $Q_{ca} \downarrow$), the height of peak ①, ② and ③ drop and the location of the peak ① move to higher voltage. The peak value drop of ①, ② or ③ is marked as $P1 \downarrow$, $P2 \downarrow$ and $P3 \downarrow$, respectively, as in Table 4. The location move to the higher voltage of peak ① is marked as $P1 \rightarrow$ in Table 4. Fig. 15(e) and (f) show that when Q_{an} decreases (marked as $Q_{an} \downarrow$), peak ①, ② drop then disappear. The peaks ③ + II and ③ + I form an M-type in the IC curve when Q_{an} decreases to 40% or less of its original value. The drop and disappear behavior of the peak ① and ② is marked as $P1 \downarrow$ -D and $P2 \downarrow$ -D, respectively, as in Table 4. The appearance (disappearance) of the M-type in IC curve is marked as MA (MD) in Table 4. Fig. 15(g) and (h) show that when y_0 increases (marked as $y_0 \uparrow$), peak ③ and III disappear. The peak locations tend to converge to 3.6 V. The disappearance of peak ③ is marked as $P3 \downarrow$ -D as in Table 4. The convergence for the peak locations is marked as SC as in Table 4. Fig. 15(i) and (j) show that when x_0 decreases (marked as $x_0 \downarrow$), peak ①, ② and I drop then disappear. And peak ③ + III and ③ + II form an M-type in the IC curve when x_0 is less than 0.4. A plateau can be seen <3.5 V, which is a unique characteristic caused by the decrease of x_0 . The plateau rising at voltage lower than 3.5 V is defined as PL↑ marked in Table 4.

Table 5 concludes the characteristics of the IC curves for different degradation (recovery) mechanisms shown in Fig. 15.



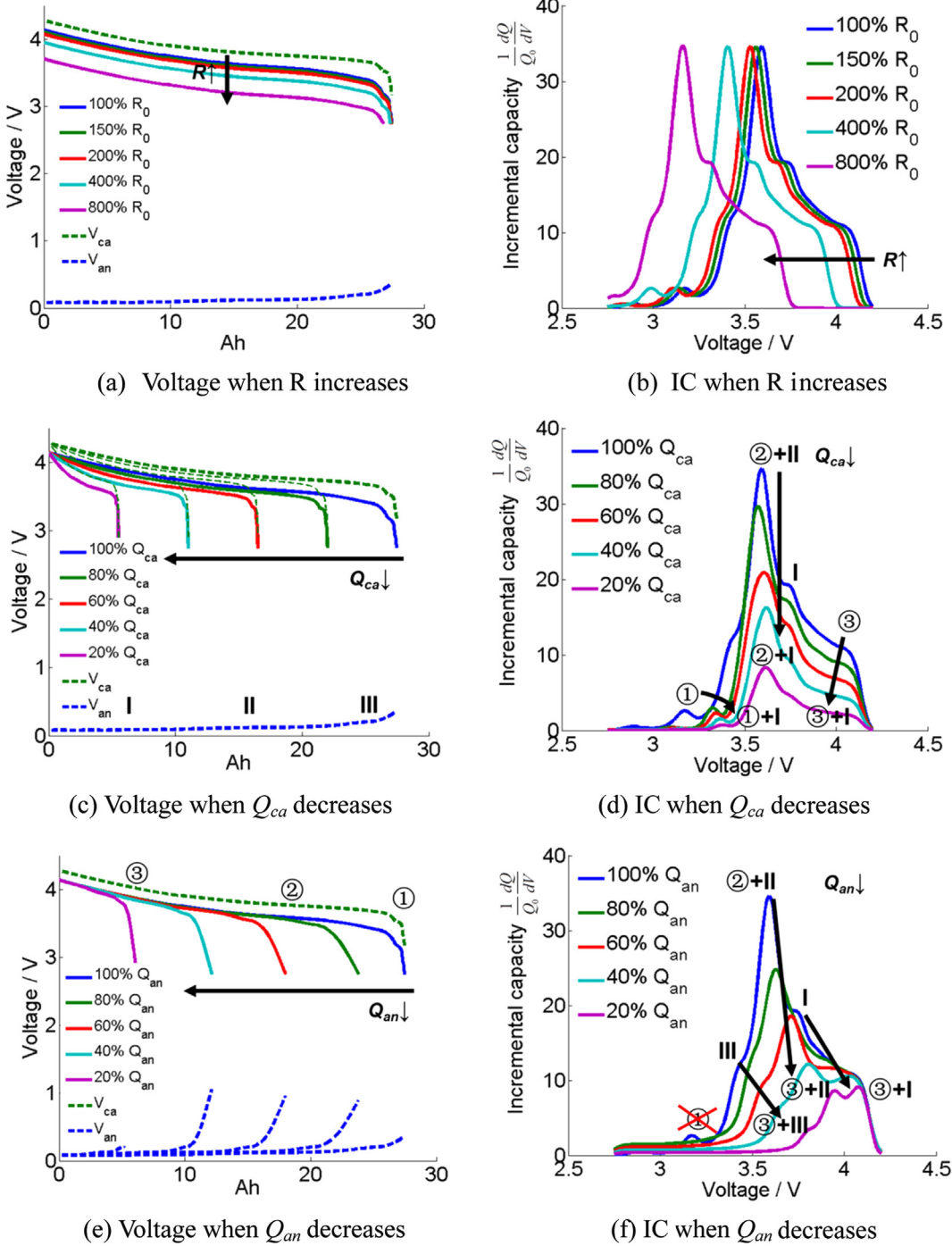


Fig. 15. The influence of the parameters used in the mechanistic model on the IC curves.

Characteristics of the IC curve changes from the before-heating cycle to the first discharge cycle after cooling for $T_{cool} = 120^\circ\text{C}$ (Fig. 12(e)) and $T_{cool} = 130^\circ\text{C}$ (Fig. 12(f)) have been collected in Table 6. The degradation mechanism can be inferred comparing with the characteristics of the IC curves listed in Tables 5 and 6. During high temperature exposure, the $R \uparrow$ and the $x_0 \downarrow$ can be confirmed, because only the $R \uparrow$ can cause SL, and only the $x_0 \downarrow$ can cause PL \uparrow , see Table 5. The $x_0 \downarrow$ indicates the LLI at the anode, as discussed in Refs. [38–44]. An M-type IC curve can be seen for the first discharge cycle of the battery with $T_{cool} = 130^\circ\text{C}$ (MA). The MA can be caused by both the $Q_{an} \downarrow$ and

the $x_0 \downarrow$, see Table 5. However, the $Q_{an} \downarrow$ is less likely to happen, because the anode active material does not decompose at $T < 160^\circ\text{C}$.

LAM at cathode as reported in Refs. [7,61] can be inferred using the information on IC in Tables 5 and 6. The $Q_{ca} \downarrow$ and the $y_0 \uparrow$, which both represent LAM at cathode, can both lead to P3 \downarrow while other parameters cannot. Therefore P3 \downarrow shown in Table 6 can be caused by either $Q_{ca} \downarrow$ or $y_0 \uparrow$. However, a big $y_0 \uparrow$ is less likely to happen, because a big $y_0 \uparrow$ will cause P3 \downarrow -D according to Table 5, while peak ③ can still be seen in the IC derived from experiment results.

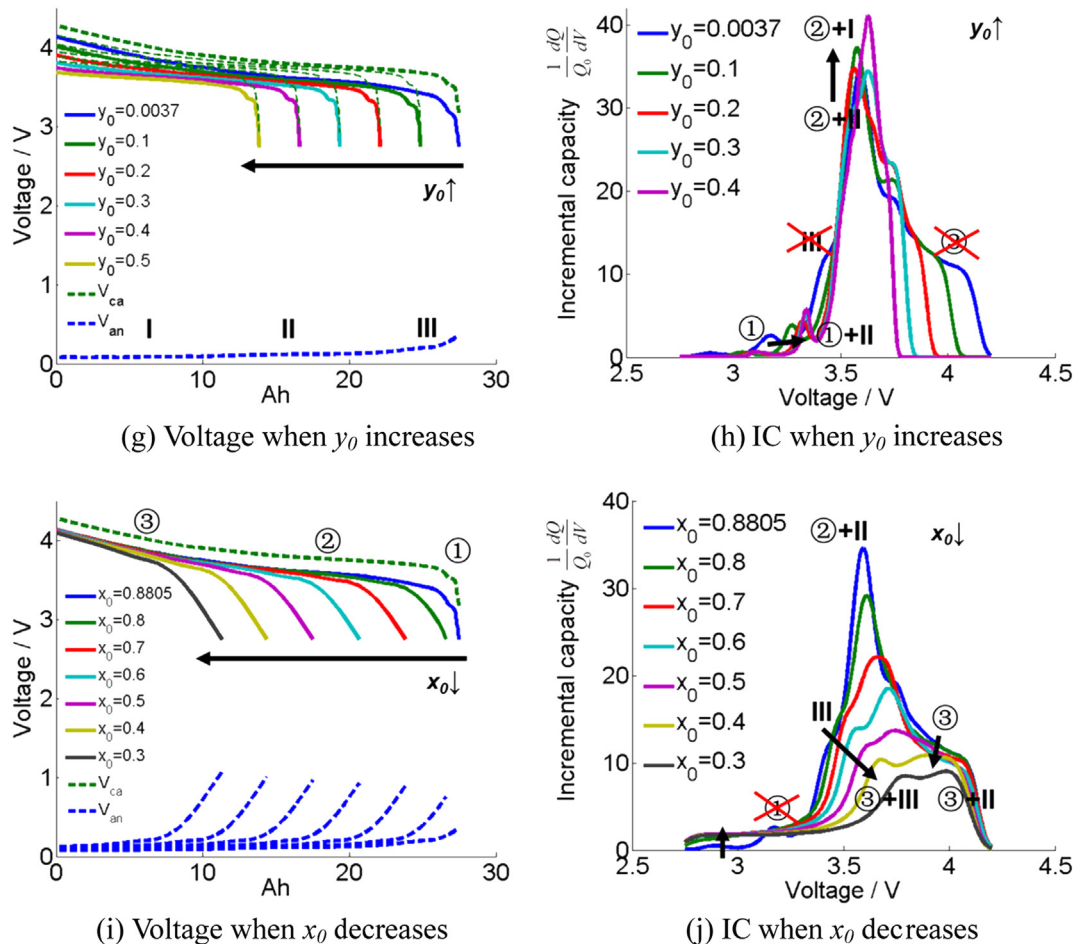


Fig. 15. (continued).

The recovery characteristics of the IC variation from the first cycle after cooling to the last cycle after cooling for $T_{cool} = 120^\circ\text{C}$ (Fig. 12(e)) and $T_{cool} = 130^\circ\text{C}$ (Fig. 12(f)) can also be inferred from Tables 5 and 6. SH during recovery indicates the $R \downarrow$, while the disappearance of M-type (MD) indicates $x_0 \uparrow$ during the capacity recovery process. Meanwhile, P2↑ and P3↑ indicate a recovery of the active material loss at the cathode.

Table 4
Descriptions for the abbreviations used in Tables 5 and 6.

Abbreviations of characteristics	Descriptions
Curve shift	SL (SH) SC
For peak ①	P1↓ (P1↑) P1↓-D P1→ (P1←)
For peak ②	P2↓ (P2↑) P2↓-D
For peak ③	P3↓ (P3↑) P3↓-D
M-type Plateau <3.5 V	MA (MD) PL↑ (PL↓)
	The peak locations in the IC curve shift to lower (higher) voltage. The peak locations in the IC curve converge to center. The height of peak ① drops (rises). The height of peak ① drops, then peak ① disappears. The location of peak ① moves to higher (lower) voltage. The height of peak ② drops (rises). The height of peak ② drops, then peak ② disappears. The height of peak ③ drops (rises). The height of peak ③ drops, then peak ③ disappears. The M-type appears (disappears). A plateau lower than 3.5 V rises (drops).

Table 5
Characteristics of the IC curve changes under different degradation mechanisms.

Case	Characteristics of the IC curve changes	
Degradation	$R \uparrow$	SL
	$Q_{ca} \downarrow$	P1↓, P2↓, P3↓, P1→
	$Q_{an} \downarrow$	P1↓-D, P2↓-D, MA
	$y_0 \uparrow$	P3↓-D, SC, P1→
	$x_0 \downarrow$	P1↓-D, P2↓-D, MA, PL↑
	$R \downarrow$	SH
	$Q_{ca} \uparrow$	P1↑, P2↑, P3↑, P1←
	$Q_{an} \uparrow$	P1↑, P2↑, MD
	$y_0 \downarrow$	P3↑, P1←
	$x_0 \uparrow$	P1↑, P2↑, MD, PL↓
Recovery	$R \uparrow$	SL
	$Q_{ca} \downarrow$	P1↓, P2↓, P3↓, P1→
	$Q_{an} \downarrow$	P1↓-D, P2↓-D, MA
	$y_0 \uparrow$	P3↓-D, SC, P1→
	$x_0 \downarrow$	P1↓-D, P2↓-D, MA, PL↑
	$R \downarrow$	SH
	$Q_{ca} \uparrow$	P1↑, P2↑, P3↑, P1←
	$Q_{an} \uparrow$	P1↑, P2↑, MD
	$y_0 \downarrow$	P3↑, P1←
	$x_0 \uparrow$	P1↑, P2↑, MD, PL↓

Table 6
Characteristics of the IC curve changes for $T_{cool} = 120^\circ\text{C}$ and 130°C .

Case	Characteristics
Degradation	$T_{cool} = 120^\circ\text{C}$, change from "before heating" SL, PL↑, P1↓-D, to "after 1st cycle", Fig. 12(e) P2↓, P3↓
	$T_{cool} = 130^\circ\text{C}$, change from "before heating" SL, PL↑, MA, P1↓-D, to "after 1st cycle", Fig. 12(f) P2↓, P3↓
	$T_{cool} = 120^\circ\text{C}$, change from "after 1st cycle" SH, P2↑, P3↑ to "after last cycle", Fig. 12(e) P2↓, P3↓
Recovery	$T_{cool} = 130^\circ\text{C}$, change from "after 1st cycle" SH, MD, P2↑, P3↑ to "after last cycle", Fig. 12(f) P2↓, P3↓

4. Conclusion

A follow-up study of [9] is provided in this paper to analyze the fading mechanisms of a 25 Ah NCM battery exposed to extreme temperature but without thermal runaway during an EV-ARC test. Series of EV-ARC tests with early termination were conducted by heating the sample battery to several temperature levels below thermal runaway.

Reusability of the batteries after exposed to extreme temperatures or near runaway condition is investigated. The range for the terminal temperature that the battery can be exposed to and still remains useful is determined. The experimental data reveal that the melting point of the separator dictates the reusability of the 25 Ah NCM battery. The battery capacity may partly recover through several discharge/charge cycles, but some of the capacity loss is permanent.

The capacity fading mechanisms are studied using incremental capacity analysis (ICA). In addition, the fading mechanism and the capacity recovery behavior are analyzed using a mechanistic model. The increase of the resistance, loss of lithium inventory (LLI) in anode and the loss of active material (LAM) in cathode can be confirmed by comparing the IC curves derived from the experimental data with the IC curves derived from the mechanistic model.

Future work will focus on quantifying the capacity loss at the cathode and anode to provide quantitative data to calibrate a thermal-electrochemical model that can predict both the voltage and the temperature simultaneously.

Acknowledgment

This work is funded by US-China Clean Energy Research Center-Clean Vehicle Consortium (CERC-CVC), and the MOST (Ministry of Science and Technology) of China under the contract of No. 2014DFG71590. The first author is funded by China Scholarship Council.

The first author appreciates the substantial discussions and suggestions by Mr. Caihao Weng and other co-workmates in the RACE Lab. The author would like to thank Mr. Maogang Li (from Thermal Hazard Technology), Mr. Hengwei Liu and Ms. Xiaoyi Xie for the experiment support. Gratitude should be also given to Mr. Jinguo Cheng in Advanced Energy for providing physical data of the battery.

References

- [1] Q.S. Wang, P. Ping, X. Zhao, G. Chu, J. Sun, C. Chen, *J. Power Sources* 208 (2012) 210–224.
- [2] Garrett P. Beauregard, Report of Investigation: Hybrids Plus Plug in Hybrid Electric Vehicle, eTec, Phoenix AZ, 2008.
- [3] B. Smith, Chevrolet Volt Battery Incident Overview Report, U.S. Department of Transportation, National Highway Traffic Safety Administration, 2012, p. 1.
- [4] K.J. Lee, K. Smith, A. Pesaran, G.H. Kim, *J. Power Sources* 241 (2013) 20–32.
- [5] G.H. Kim, A. Pesaran, R. Spotnitz, *J. Power Sources* 170 (2007) 476–489.
- [6] H. Zheng, Q. Sun, G. Liu, X. Song, V.S. Battaglia, *J. Power Sources* 207 (2012) 134–140.
- [7] W. Liu, M. Wang, J. Chen, X. Zhang, H. Zhou, *J. Electrochem.* 18 (2) (2012) 118–124 (in Chinese).
- [8] D.H. Doughty, Vehicle Battery Safety Roadmap Guidance, Oct. 2012, pp. 65–66.
- [9] X. Feng, M. Fang, X. He, M. Ouyang, L. Lu, H. Wang, M. Zhang, *J. Power Sources* 255 (2014) 294–301.
- [10] R. Spotnitz, J. Franklin, *J. Power Sources* 113 (2003) 81–100.
- [11] T.M. Bandhauer, S. Garimella, T.F. Fuller, *J. Electrochem. Soc.* 158 (3) (2011) 1–25.
- [12] D. Lisbona, T. Snee, *Process Saf. Environ. Prot.* 89 (2011) 434–442.
- [13] J. Wen, Y. Yu, C. Chen, *Mater. Express* 2 (3) (2012) 197–212.
- [14] L. Lu, X. Han, J. Li, J. Hua, M. Ouyang, *J. Power Sources* 226 (2013) 272–288.
- [15] M.N. Richard, J.R. Dahn, *J. Electrochem. Soc.* 146 (6) (1999) 2068–2077.
- [16] D.D. Macneil, D. Larcher, J.R. Dahn, *J. Electrochem. Soc.* 146 (10) (1999) 3596–3602.
- [17] H. Maleki, G. Deng, A. Anani, J. Howard, *J. Electrochem. Soc.* 146 (9) (1999) 3224–3229.
- [18] M.H. Ryoo, J.N. Lee, D.J. Lee, W. Kim, Y.K. Jeong, J.W. Choi, J. Park, Y.M. Lee, *Electrochim. Acta* 83 (2012) 259–263.
- [19] Q.S. Wang, J. Sun, X. Yan, C. Chen, *Thermochim. Acta* 487 (2005) 12–16.
- [20] M. Zhou, L. Zhao, S. Okada, J. Yamaki, *J. Electrochem. Soc.* 159 (1) (2012) A44–A48.
- [21] J. Yamaki, H. Takatsui, T. Kawamura, M. Egashira, *Solid State Ionics* 148 (2002) 241–245.
- [22] P. Biensan, B. Simon, J.P. Peres, A. Guibert, M. Broussely, J.M. Bodet, F. Perton, *J. Power Sources* 81–82 (1999) 906–912.
- [23] Z. Zhang, D. Fouchard, J.R. Rea, *J. Power Sources* 70 (1998) 16–20.
- [24] D.D. Macneil, J.R. Dahn, *J. Phys. Chem. A* 105 (2001) 4430–4439.
- [25] H. Arai, M. Tsuda, K. Saito, M. Hayashi, Y. Sakurai, *J. Electrochem. Soc.* 149 (4) (2002) 401–406.
- [26] H.Y. Wang, A.D. Tang, K.L. Huang, *Chin. J. Chem.* 29 (2011) 1583–1588.
- [27] H. Kim, M. Kong, K. Kim, I. Kim, H. Gu, *J. Power Sources* 171 (2007) 917–921.
- [28] H. Kim, K. Kim, S.I. Moon, I. Kim, H. Gu, *J. Solid State Electrochem.* 12 (2008) 867–872.
- [29] I. Belharouak, Y.K. Sun, J. Lin, K. Amine, *J. Power Sources* 123 (2003) 247–252.
- [30] J. Jiang, K.W. Eberman, L.J. Krause, J.R. Dahn, *J. Electrochem. Soc.* 152 (3) (2005) 566–569.
- [31] Y.H. Chen, Investigation on $\text{LiCo}_{1/3}\text{Ni}_{1/3}\text{Mn}_{1/3}\text{O}_2$ Cathode Material and Safety of Lithium-ion Battery, Ph. D Thesis, Tianjin: College of Chemical Engineering, Tianjin University, China, 2006, 12, pp50, (in Chinese).
- [32] P. Roeder, N. Baba, H.D. Wiemhoefer, *J. Power Sources* 248 (2014) 978–987.
- [33] K. Takei, K. Kumai, Y. Kobayashi, H. Miyashir, N. Terada, T. Iwahori, T. Tanaka, *J. Power Sources* 97–98 (2001) 697–701.
- [34] R.D. Ramasamy, R.E. White, B.N. Popov, *J. Power Sources* 141 (2005) 298–306.
- [35] K. Amine, J. Liu, S. Kang, I. Belharouak, Y. Hyung, D. Vissers, G. Henriksen, *J. Power Sources* 129 (2004) 14–19.
- [36] K. Amine, J. Liu, I. Belharouak, *Electrochim. Commun.* 7 (2005) 669–673.
- [37] T. Yoshida, M. Takahashi, S. Morikawa, C. Ihara, H. Hatsukawa, T. Shiratsuchi, J. Yamaki, *J. Electrochem. Soc.* 153 (3) (2006) A576–A582.
- [38] J. Christensen, J. Newman, *J. Electrochem. Soc.* 105 (11) (2003) A1416–A1420.
- [39] J. Christensen, J. Newman, *J. Electrochem. Soc.* 152 (4) (2005) A818–A829.
- [40] Q. Zhang, R.E. White, *J. Power Sources* 173 (2007) 990–997.
- [41] Q. Zhang, R.E. White, *J. Power Sources* 179 (2008) 785–792.
- [42] Q. Zhang, R.E. White, *J. Power Sources* 179 (2008) 793–798.
- [43] M. Dubarry, C. Truchot, B.Y. Liaw, *J. Power Sources* 219 (2012) 204–216.
- [44] X. Han, M. Ouyang, L. Lu, J. Li, Y. Zheng, Z. Li, *J. Power Sources* 251 (2014) 38–54.
- [45] J.H. Kim, N. Pieczonka, Z. Li, Y. Wu, S. Harris, B.R. Powell, *Electrochim. Acta* 90 (2013) 556–562.
- [46] K. Honkura, K. Takahashi, T. Horiba, *J. Power Sources* 196 (2011) 10141–10147.
- [47] H.M. Dahn, A.J. Smith, J.C. Burns, D.A. Stevens, J.R. Dahn, *J. Electrochem. Soc.* 159 (9) (2012) A1405–A1409.
- [48] I. Bloom, A.N. Jansen, D.P. Abraham, J. Knuth, S.A. Jones, V.S. Battaglia, G.L. Henriksen, *J. Power Sources* 139 (2005) 295–303.
- [49] I. Bloom, J.P. Christophersen, K. Gering, *J. Power Sources* 139 (2005) 304–313.
- [50] I. Bloom, L.K. Walker, J.K. Basco, D.P. Abraham, J.P. Christophersen, C.D. Ho, *J. Power Sources* 195 (2010) 877–882.
- [51] M. Dubarry, V. Svoboda, R. Hwu, B.Y. Liaw, *J. Power Sources* 165 (2007) 566–572.
- [52] M. Dubarry, V. Svoboda, R. Hwu, B.Y. Liaw, *J. Power Sources* 174 (2007) 1121–1125.
- [53] M. Dubarry, C. Truchot, M. Cugnet, B.Y. Liaw, K. Gering, S. Sazhin, D. Jamison, C. Michelbacher, *J. Power Sources* 196 (2011) 10328–10335.
- [54] M. Dubarry, C. Truchot, B.Y. Liaw, K. Gering, S. Sazhin, D. Jamison, C. Michelbacher, *J. Power Sources* 196 (2011) 10336–110343.
- [55] M. Dubarry, B.Y. Liaw, *J. Power Sources* 194 (2009) 541–549.
- [56] M. Dubarry, B.Y. Liaw, M.S. Chen, S. Chyan, K. Han, W. Sie, S. Wu, *J. Power Sources* 196 (2011) 3420–3425.
- [57] C. Weng, Y. Cui, J. Sun, H. Peng, *J. Power Sources* 235 (2013) 36–44.
- [58] C. Weng, J. Sun, H. Peng, *J. Power Sources* 258 (2014) 228–237.
- [59] X. Feng, J. Li, M. Ouyang, L. Lu, J. Li, X. He, *J. Power Sources* 232 (2013) 209–218.
- [60] T. Ohzuku, Y. Iwakoshi, K. Sawai, *J. Electrochem. Soc.* 140 (9) (1993) 2490–2498.
- [61] Y.K. Sun, S.T. Myung, C.S. Yoon, D.W. Kim, *Electrochim. Solid State Lett.* 12 (8) (2009) A163–A166.